Prediction-Based Method for Micropipette Approaching to Optimal Spindle Removal Position

Zuqi Wang, Yujie Zhang, Yidi Zhang, Detian Zhang, Zhaotong Chu, Qili Zhao, *Member, IEEE*, Mingzhu Sun, *Member, IEEE*, Maosheng Cui, Xin Zhao, *Member, IEEE*, and Yaowei Liu, *Member, IEEE*

***Abstract*— During somatic cell nuclear transfer (SCNT), precise removal of the oocyte genetic material is critical. However, due to the invisibility of the genetic material (spindle) under brightfield observation and the potential displacement caused by the movement of micropipettes, accurately positioning the micropipette at the spindle poses a significant challenge. This study introduces an approach for optimal spindle removal by predicting its position. Initially, the polarization imaging system visualized the oocyte spindle, while a Multi-Feature Adaptive Kernel Correlation Filter (MFAKCF) algorithm tracked the spindle with 92.84% accuracy. Subsequently, enhancements were made to the Nonlinear Mass-Spring-Damper (NMSD) model to simulate live oocyte mechanical characteristics. Adjustments to NMSD model parameters simulated spindle displacement variations under diverse experimental conditions. Finally, the optimal spindle removal position was determined using NMSD model to simulate the micropipette approach to the spindle and the resulting position of spindle displacement. Experimental validation showed that the predictive accuracy of this model was 97.26%, with an average positional error of 0.4 μm. Using this approach method can reduce cytoplasm loss to 4.5% and have a 100% enucleation success rate. Thus, the proposed prediction based optimal spindle removal position method can effectively anticipates spindle final positions, aiding in minimizing cytoplasmic loss during spindle removal.**

Received 21 August 2024; revised 23 December 2024; accepted 25 January 2025. Date of publication 29 January 2025; date of current version 11 April 2025. This article was recommended for publication by Associate Editor H. Wang and Editor J. Yi upon evaluation of the reviewers' comments. This work was supported in part by the National Natural Science Foundation of China under Grant 62333012 and Grant 62273185; in part by the Young Scientific and Technological Talents (Level Three), Tianjin; in part by Shenzhen Science and Technology Innovation Commission, China, under Project SGDX2020110309300502; and in part by Guangdong Basic and Applied Basic Research Foundation under Grant 2022A1515010107. *(Corresponding author: Yaowei Liu.)*

This work involved human subjects or animals in its research. Approval of all ethical and experimental procedures and protocols was granted by the Committee for Animal Experimentation of the College of Life Science at Nankai University under Approval No. 2008, and performed in line with the NIH Guide for the Care and Use of Laboratory Animals (No. 8023, Revised in 1996).

Zuqi Wang, Yujie Zhang, Yidi Zhang, Detian Zhang, Zhaotong Chu, Qili Zhao, Mingzhu Sun, Xin Zhao, and Yaowei Liu are with the National Key Laboratory of Intelligent Tracking and Forecasting for Infectious Diseases and Tianjin Key Laboratory of Intelligent Robotic (tikLIR), Engineering Research Center of Trusted Behavior Intelligence, Ministry of Education, Institute of Robotics and Automatic Information System (IRAIS), Nankai University, Tianjin 300350, China, and also with the Institute of Intelligence Technology and Robotic Systems, Shenzhen Research Institute of Nankai University, Shenzhen 518083, China (e-mail: liuyaowei@nankai.edu.cn).

Maosheng Cui is with the Institute of Animal Science and Veterinary of Tianjin, Tianjin 300381, China.

Digital Object Identifier 10.1109/TASE.2025.3536036

***Note to Practitioners*—Accurate oocyte nucleus removal is crucial for somatic cell nuclear transfer (SCNT) but challenging due to spindle invisibility under brightfield microscopy and displacement caused by micropipette movements. This study proposes a predictive method to address these issues. The polarization imaging system was used to visualize the spindle, and a MFAKCF tracking algorithm enabled real-time tracking. An enhanced NMSD model simulated spindle displacement, enabling accurate position prediction and reducing cytoplasmic loss during removal. This method offers a reliable tool for precise spindle removal in SCNT and broader applications in biomedical micromanipulation.**

***Index Terms*— Robotic micro-manipulation, single cell manipulation, cell modeling, micro-vision.**

I. Introduction

SOMATIC cell nuclear transfer (SCNT) plays a crucial role in somatic cell transplantation and represents a significant technology in the field of assisted reproductive technology [1]. In recent years, the rapid development of micromanipulation robots, combined with intelligent control algorithms, has led to significant advancements in the automation of SCNT. Robotic micromanipulation technology allows for precise control of micropipettes at a microscopic scale, enabling high-precision manipulation of oocytes [2]. This technology has achieved remarkable results in cell biology, particularly in cloning [3], gene editing [4], and cell therapy [5], providing unprecedented levels of precision. The integration of intelligent control algorithms has further enhanced the accuracy and efficiency of robotic systems [6], greatly accelerating the translation from basic research to clinical applications.

Despite the potential of SCNT, a major challenge remains the precise extraction of the spindle from the oocyte cytoplasm, which often leads to unnecessary cytoplasmic loss [7]. Traditional nuclear removal methods further complicate this process due to the spindle's invisibility, as shown in Fig. 1(a). During the spindle removal process, after a glass micropipette penetrates the zona pellucida and cell membrane of the oocyte, there exists a notable distance between the micropipette's opening and the spindle, as shown in Fig. 1 (b). If the micropipette pressure is reduced at this point to transfer the spindle into the micropipette, it may cause excessive cytoplasmic loss between the micropipette's opening and the spindle. Existing studies indicate that removing excess cytoplasm

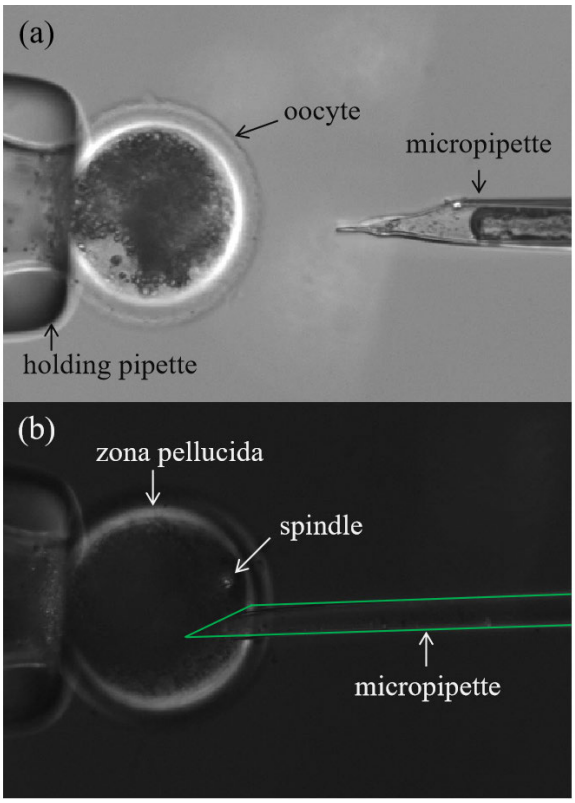

Fig. 1. Oocyte enucleation. The schematic plot shows the non-negligible distance between the micropipette opening and the nucleus.

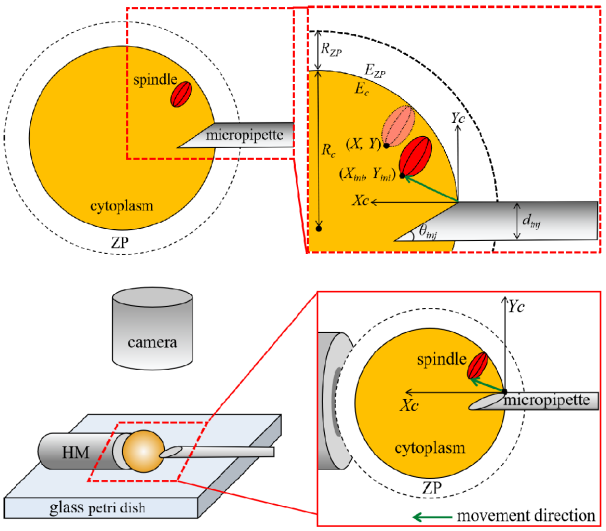

Fig. 2. The micropipette approaching the spindle will cause the spindle to move. The green arrow points to the micropipette moving to the "optimal spindle removal position", and the dashed box shows the factors affecting the displacement distance and direction.

significantly impacts the subsequent development of oocytes [8]. To address this challenge, our study proposes a comprehensive approach, including precise spindle positioning, prediction of spindle migration, and direct control of micropipette movement to the spindle migrate position. These measures aim to enhance the developmental potential of cloned embryos by minimizing cytoplasmic loss to the greatest extent possible.

Precise spindle localization is crucial for accurate removal. Recent studies have advanced beyond traditional invisible aspiration techniques by incorporating fluorescent staining to differentiate polar body and cell nucleus positions [9]. Although this method significantly enhances the success rate of oocyte extraction, it only predicts the nucleus position in 54% of oocytes [10]. In contrast, another team [11] utilized the polarization imaging system to visualize the spindle during Meiosis II (MII), demonstrating innovative applications of this technology. This pioneering technology has successfully been employed in various fields such as cell sorting [12], intra-cytoplasmic sperm injection (ICSI) [13], and macaque cloning [14]. Our research represents the first application of this technology in the robotics SCNT field, utilizing spindle position information obtained from the polarization imaging system to determine the optimal spindle removal position.

Accurately locating and tracking the spindle in oocytes poses significant technical challenges due to the cell's microscopic scale, highly dynamic structural changes, and visibility issues under brightfield microscopy [15], [16]. As shown in Fig. 1(a), the spindle is difficult to image directly using brightfield microscopy, making it difficult for traditional methods such as invisible aspiration to visualize spindle and manage complex positional dynamics. Studies has shown that the precise localization of the spindle holds critical importance not only for the success of techniques like somatic cell nuclear transfer [17] but also for advancing biomedical research and applications in areas such as cloning, gene editing, and reproductive therapies [18]. Therefore, this paper addresses these challenges by proposing Multi-Features Adaptive Kernel Correlation Filters (MFAKCF), aiming to provide a robust solution to enhance spindle localization and tracking accuracy in oocytes, thereby assisting the micropipette to approach the spindle and achieve enucleation based on the optimal spindle removal position.

In MII oocytes, the viscoelasticity of the cytoplasm and the concurrent breakdown of the nuclear membrane add complexity to the movement of micropipettes [19]. As shown in Fig. 2, when a micropipette with an asymmetric tip approaches the spindle, the applied forces cause spindle displacement, which is influenced by various experimental parameters, such as oocyte diameter R_c, zona pellucida length R_{zp}, micropipette width d_{inj}, Young's modulus of the oocyte E_c and Young's modulus of the zona pellucida E_{zp}. To elucidate the intricate dynamics between micropipette parameters, oocyte morphology, and motion conditions affecting the end-point positioning of genetic material, modeling approaches are crucial. Previous studies [20], [21] successfully simulated millimeter-scale soft tissue deformation after compression using Mass-Spring-Damper (MSD) systems, achieving significant results. However, oocytes typically range in size from 120 μm to 150 μm with more complex mechanical properties.

Addressing this, we propose an advanced Nonlinear Mass-Spring-Damper (NMSD) model by expanding the spring constant into a piecewise expression: employing a cubic polynomial for low displacements and a linear function for high displacements. Furthermore, enhancing the damper's

characteristics enhances the model's ability to capture viscoelastic behavior, integrating the effects of strain rate beyond traditional linear methods. Building on precise modeling, we simulate micropipette approach to the spindle in a virtual environment, obtaining coordinates of the displaced spindle position (optimal removal position), and subsequently validate through experimental control of micropipette approach to these coordinates, successfully achieving prediction-based optimal spindle removal position experiments.

Compared with the existing works, the contributions of this paper are summarized as follows: (1) Development of the Multi-Feature Adaptive Kernel Correlation Filter (MFAKCF) algorithm, achieving 92.84% spindle tracking accuracy and a 100% success rate under challenging imaging conditions. (2) A improved Nonlinear Mass-Spring-Damper (NMSD) model that accurately predicted spindle displacement, with an average error of 0.4 μm. (3) A prediction-based optimal spindle removal method, reducing cytoplasmic loss to 4.5% compared to 6.9% with traditional methods. Experimental validation using 60 porcine oocytes, demonstrating the reproducibility and effectiveness of the proposed method in improving SCNT outcomes.

The remainder of this paper is structured as follows: Section II presents essential technologies and methodologies for achieving the optimal removal position of the spindle with micropipettes. This includes techniques such as spindle localization under polarized light, the development of tracking algorithms tailored to these conditions, and the predictive approach using the NMSD model. Section III details the experimental protocols, covering both spindle tracking results and spindle displacement predictions. In Section IV, the implications of these research findings for somatic cell nuclear transfer are explored, alongside suggestions for future research directions. Finally, Section V provides the concluding remarks for this study.

II. Key Method and Technology

A. The Location of Spindle Recognition and Tracking in Polarized Image

As shown in Fig. 1(b), the spindle structure within the oocyte appears small and exhibits blurred imaging boundaries under polarized light microscopy. Our experiments reveal dynamic changes in spindle position and shape during micropipette approach for precise enucleation. Furthermore, the brightness of microscope illumination significantly influences spindle visibility. Additionally, unexpected lipid droplet occurrences in oocytes under polarized light necessitate a robust and precise tracking system [17]. Therefore, we opted for the Multi-Features Adaptive Fusion Kernel Correlation Filters (MAFKCF) for spindle detection and tracking.

Algorithm 1 outlines the recognition and tracking processes. Expanding on previous work [18], the efficacy of the KCF algorithm in accurately localizing and tracking genetic material (nuclei) in fluorescently stained oocytes has been demonstrated. KCF's circulant matrix and dense sampling techniques expedite tracking algorithms and improve feature capture, ensuring compatibility with real-time biological

Algorithm 1 Enhanced Adaptive Kernel Correlation Filter

Input: Initial frame image I_0, target bounding box B_0.
Output: Sequence of target positions $\{B_1, B_2, \ldots, B_t\}$.

$\varphi(I_0, B_0) = \omega^0_{hog} * \varphi^0_{hog} + \omega^0_{gray} * \varphi^0_{gray} \rightarrow$ Initial target feature I_0;
$\widehat{\varphi}(I_0, B_0) \rightarrow$ Fourier transform of target feature;
$H_0 \rightarrow$ Kernelized correlation filter initialized with $\widehat{\varphi}(I_0, B_0)$;
for each $i \in [1, t]$ **do**
  $\varphi(I_i, B_i) = \omega^i_{hog} * \varphi^i_{hog} + \omega^i_{gray} * \varphi^i_{gray} \rightarrow$ Extract features from frame I_i;
  $G_i \rightarrow H_{i-1} \bullet \widehat{\varphi}(I_i, B_i) \rightarrow$ Compute response map;
  $B_i \rightarrow$ Update target position based on G_i;
  $\widehat{\varphi}(I_i, B_i) \rightarrow$ Extract features from updated B_i;
  $H_i \rightarrow$ Update filter with $\widehat{\varphi}(I_i, B_i)$;
end for
return $B = \{B_1, B_2, \ldots, B_t\}$.

experiments [19]. In this research, we adapted the method for use with polarized images. Initially, we integrated multi-feature adaptive fusion capabilities that combine grayscale histogram and HOG features to segment the spindle area and fortify the algorithm against microscope light variations. Secondly, a template adaptive update mechanism was introduced to mitigate the influence of lipid droplets during experimental procedures. The combined enhancements result in a comprehensive tracking system capable of dynamically and accurately following the oocyte spindle under polarized light conditions.

B. Oocyte Modeling Based on NMSD Model

Obtaining an accurate model to simulate the mechanical properties of the oocyte is a prerequisite for obtaining the spindle position migration coordinates. In this section, we firstly model the oocyte mechanical properties with the NMSD model, and then use the force-displacement curves to calibrate the model parameters, and finally obtain a model of the oocyte mechanical properties that takes into account both the accuracy and the fast response characteristics.

1) NMSD Mechanical Model: A large number of studies have been conducted to elucidate the complexity of the mechanical properties of living oocytes, which are mainly characterized by incompressibility, isotropy, and time-velocity dependence [20], [21]. Among various simulation methods available (such as finite element [22], material point [23], and MSD [24]), we enhanced the NMSD model due to its modular flexibility in handling mechanical interactions at the pipette/cell interface across different cell geometries.

In our simulation environment, the oocyte focal plane is modeled as shown in the Fig.3, with each mass connected to the surrounding masses in a Voigt form, i.e., springs and dampers connected in parallel. This innovative approach effectively models stress relaxation and reversible deformation in live oocytes [25], offering a new framework for describing viscoelastic behavior in active cells. According to Newton's second law of motion and Hooke's law, the force equation of

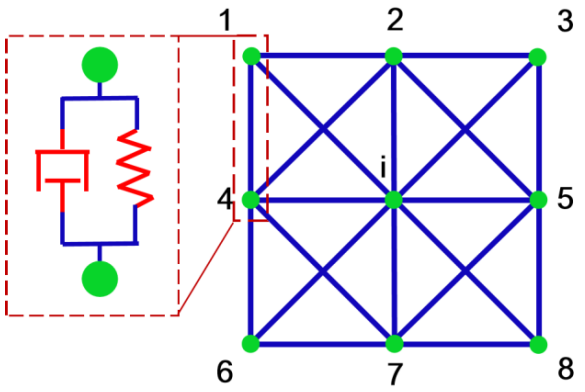

Fig. 3. Schematic diagram of the MSD model. The Voigt connection is shown schematically in the dashed box.

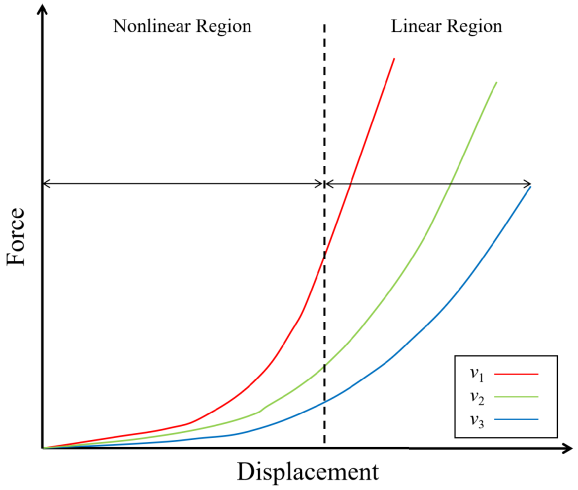

Fig. 4. The typical force-displacement behavior of living oocytes for different squeezing velocities v_1>v_2>v_3.

the proposed model is:

$$M_i\ddot{r}_i + F_i^k + F_i^d = F_i^{ext} \tag{1}$$

in which M_i and r_i are the mass and position vector at node i; F_i^k, F_i^d and F_i^{ext} denote the spring force, damping force and externally applied force on node i, respectively.

To capture the highly nonlinear elastic behavior of live oocytes (as shown in Fig. 4.), we extended the representation of the spring in the NMSD model. According to Hooke's law, the force expression for spring deformation F_i^k is:

$$F_i^k = \sum_{j=1}^{N} K_{ij} \frac{r_i - r_j}{\|r_i - r_j\|} \tag{2}$$

among them, K_{ij} is the calculation formula of spring constant, $\frac{r_i - r_j}{\|r_i - r_j\|}$ is the length change of spring between node i and node j.

This extension employs a two-step approach to represent the force-displacement characteristic: a third-degree polynomial at low displacements and a transition to linear behavior at high displacements.

$$\begin{aligned} K_{ij} &= k_1\Delta l_{ij} + k_2\Delta l_{ij}^3, \left|\Delta l_{ij}\right| \le |\Delta l_c| \\ &\quad \mathbf{or}\left[A + B\left(\left|\Delta l_{ij}\right| - |\Delta l_c|\right)\right]\mathbf{sgn}\left(\Delta l_{ij}\right), \left|\Delta l_{ij}\right| > |\Delta l_c| \end{aligned} \tag{3}$$

Algorithm 2 Nonlinear Mass Spring Damper Model

Initialization: $r_i, \dot{r}_i, m_i, F_i^k, F_i^d$, for $i = 0, \ldots, N\text{-}l$;
loop
  do
    Obtain the external forces F_i^{ext} or position-based attachment from the instrument;
    Compute the spring forces F_i^k from (2)(3)(4)(5);
    Compute the damper forces F_i^d from (6);
    Estimate the resultant forces from (1);
    Compute the positions and velocities;
    Update the positions $r_i(t + \Delta t) \to r_i$ and velocities $\dot{r}_i(t + \Delta t) \to \dot{r}_i$.
  end
end loop

Defining the model parameters for the enhanced spring behavior:

· k_1: Nonlinear spring stiffness.

· k_2: Linear spring stiffness.

· Δl_{ij}: Length changes of the spring connecting nodes i and j.

· l_c: Critical displacement, below which springs exhibit nonlinear behavior.

· Parameters A and B: Constants, defined as follows:

$$A = K_1\Delta l_c + K_2\Delta l_c^3 \tag{4}$$

$$B = K_1 + 3K_2\Delta l_c^2 \tag{5}$$

To better simulate the viscoelastic behavior of living oocytes, we extended Eq. (1) to incorporate nodal damping forces. This extension introduced a displacement-velocity component alongside the conventional velocity component, reflecting the combined influence of strain and strain rate on the model's damping characteristics.

$$F_i^d = d_0\dot{r}_i + d_1\left\|r_i - r_i^0\right\|\dot{r}_i \tag{6}$$

where d_0 and d_1 are two damping constants and r_i^0 represents the rest position of node i. Thus, the spring stiffness is a cubic polynomial at low displacements and linear at high displacements, and this direct velocity damping force on the point mass mimics viscoelasticity. Algorithm 2 summarizes the order of operations of the model.

This improved damping force expression can more accurate describe the viscoelastic response of living oocytes when subjected to external forces. Specifically, it takes into account the nonlinear behavior at low displacement and the linear behavior at high displacement, as well as the effects of strain rate on the damping characteristics. By adjusting the values of d_0 and d_1, we can better match the experimental data and thus improve the prediction accuracy of the model.

2) Identification of NMSD Model Parameters: The challenge posed by the NMSD model lies in accurately determining parameters that replicate the mechanical behavior of living oocytes. Key parameters such as k_1, k_2, d_0, and d_1, which are crucial for understanding oocyte mechanical properties, require precise definition. Our experimental findings illustrate the oocyte's force-displacement curve, revealing nonlinear

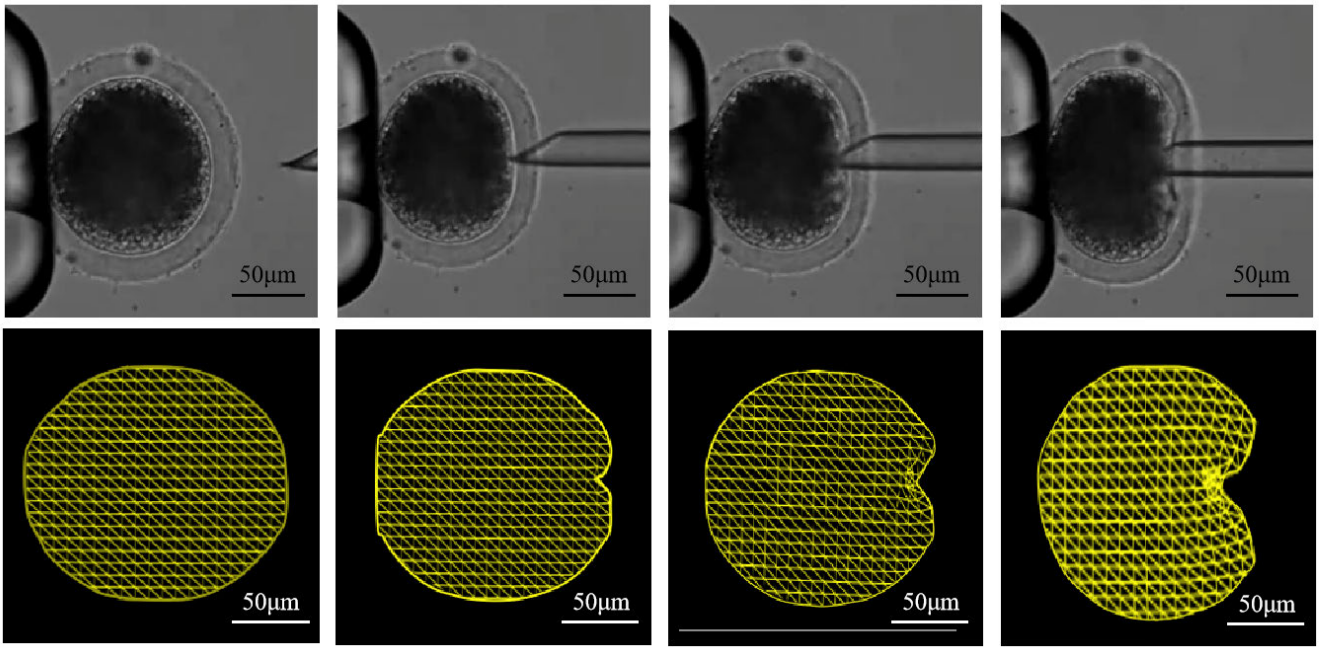

Fig. 5. Penetration experiments in real and NMSD simulated environments. The penetration depths are 0, 15, 30, and 45 μm.

characteristics at low displacements and a nearly linear relationship at higher displacements, as depicted in the Fig. 4. To ensure simulation fidelity with real-world observations, we refine NMSD model parameters by adjusting simulated force-displacement curves based on experimental data.

Using the formula proposed by [26], we computed a realistic force-displacement curve that accurately reflects oocyte penetration dynamics. This calculation involves determining force through an improved point load model and correlating displacement with micropipette penetration depth.

Fig. 5 compared penetration experiments conducted in real and simulated environments, where the simulated oocyte consists of 231 particles forming a circular structure. Each node interacts with its 8 neighboring nodes through spring and damper forces. The NMSD model demonstrates varied force-displacement behaviors with increasing X-axis displacement rates. Specifically, force nonlinearly changes with displacement at a consistent rate, exhibiting a nonlinear phase followed by linear behavior similar to indentation results seen in live cell studies. Notably, displacement rates significantly influence the mechanical responses of the model, indicating stiffer responses at higher rates, consistent with findings in biological tissue investigations [27].

Among model parameters, spring stiffness constants (e.g., k_1, k_2) prominently dictate force-deformation characteristics in respective nonlinear and linear regions. Conversely, damping parameters (e.g., d_0, and d_1) minimally influence curves at small and large deformations, respectively.

To bridge the gap between simulation and experimental results, we propose a refined optimization method aimed at adapting our model to a specific dataset. The objective function $F_{(x)}$ is formulated as the sum of squared differences between experimental data points and simulated responses. The formula for the objective function $F_{(x)}$ is:

$$F_{(x)} = (f_{x1} - f_{e1})^2 + (f_{x2} - f_{e2})^2 + \ldots\ldots + (f_{xn} - f_{en})^2 \tag{7}$$

in which f_{x1}, f_{x2} to f_{xn} are the external force values at different times obtained by NMSD model, and f_{e1}, f_{e2} to f_{en} are the actual forces obtained from the experiment at the corresponding time of the simulation data.

The $F_{(x)}$ algorithm for constrained nonlinear minimization is designed to iteratively adjust model parameters to find an optimal configuration that aligns with experimental observations. A key component of this algorithm is its ability to handle constraints, which are integral to ensuring that the parameter adjustments do not violate specific conditions required by the problem. The algorithm adjusts the parameters in each iteration while continuously checking compliance with the constraints, effectively balancing the need to minimize the objective function with the need to satisfy the constraints. This iterative adjustment process continues until the algorithm converges to an optimal parameter setup that not only minimizes the objective function but also satisfies all imposed constraints, thereby aligning closely with the experimental behavior observed. Through this rigorous iterative process, the $F_{(x)}$ algorithm ensures that the final parameter configuration is both optimal and feasible, adhering to the constraints defined by Eq.(8) and reflecting the underlying physical or experimental requirements.

$$\begin{aligned} \min \quad & F_{(x)} = f(k_1, k_2, d_0, d_1) \\ \text{s.t.} \quad & d_0 \geq 0 \\ & d_1 \geq 0 \\ & k_2 \geq 50k_1 \end{aligned} \tag{8}$$

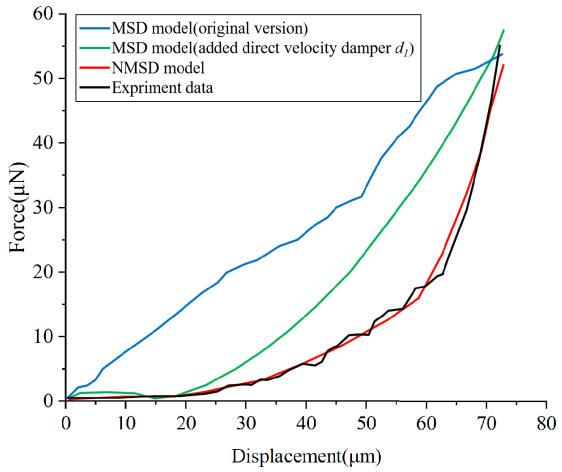

Fig. 6. Comparison of force-displacement curves obtained by different modeling methods with real experimental data.

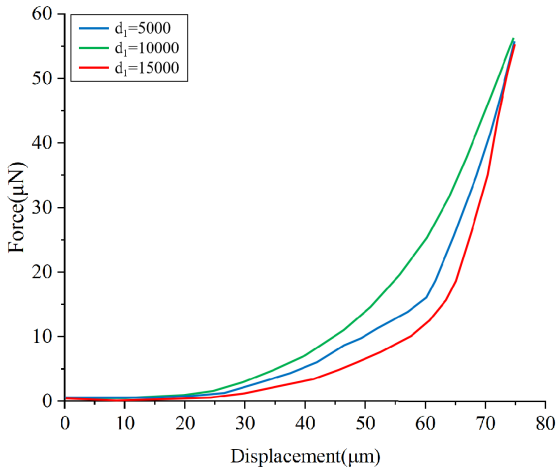

Fig. 7. Different d_1 values cause obvious changes in the force-displacement pattern of oocyte deformation under pressure.

3) Additional Parameter Necessity Verification: To better demonstrate the importance of the additional parameters (nonlinear spring constant k_1 and viscoelastic damping coefficient d_1), this study uses three different MSD systems to simulate the compression experiment on oocytes. These systems include: the original version of the MSD system [28], the MSD system with only the direct velocity damper d_0, and the NMSD system proposed in this study. By comparing the experimental data with the force-displacement curves generated by the three different modeling systems, where each curve represents the relationship between the force applied to the oocyte and the displacement during compression, the X-axis represents displacement in micrometers (μm), and the Y-axis represents force in micro-newtons (μN), several findings can be observed: In the original MSD system (which includes a linear spring and a direct velocity damper), the force-displacement curve shows negligible nonlinear behavior during the initial stage of micropipette compression (the blue curve in Fig. 6). Moreover, while adding only the direct velocity damper d_0 can partially capture the nonlinear trend in the experimental force-displacement curve (the green curve in Fig. 6), the inclusion of the viscoelastic damping coefficient d_1 significantly improved the simulation accuracy (the red curve in Fig. 6).

Fig. 7 illustrates how varying d_1 values yield discernible alterations in the force-displacement patterns of oocyte cell deformation under stress. These findings emphasize the pivotal role of k_1 and d_1 in the enhanced NMSD model, accurately depicting the intricate biomechanical traits of oocyte responses to external forces.

C. Optimal Spindle Removal Position Prediction

After obtaining an accurate NMSD model, the next step is to conduct a micropipette approaching spindle experiment in the simulation environment. The experimental process is shown in Fig. 8, and the experimental parameters are shown in the following Table I.

When the micropipette penetrated the oocyte at the 3 o'clock position of the oocyte, the online NMSD model parameter calibration is performed, where $d_0 = 20.182Ns/m$, $d_1 = 10000Nm/s^2$, $k_1 = 2.5N$, $k_2 = 95.9738N$. As shown in the Fig. 9, the oocyte puncture point is taken as the origin. After the oocyte is punctured, the micropipette approached the spindle. When the micropipette moved to the initial position $(X_{ini}, Y_{ini}) = (15.8718, 18.1392)$ of the spindle, due to the liquid properties of the cytoplasm and the squeezing force of the micropipette, the spindle moved to the offset coordinate $(X_{off}, Y_{off}) = (25.6972, 49.127)$. At this time, the obtained spindle offset coordinate (X_{off}, Y_{off}) is the optimal oocyte spindle removal point $(X_{optimal}, Y_{optimal})$, so controlling micropipette to moved from the origin to $(X_{optimal}, Y_{optimal})$ is to reached the optimal spindle removal position.

TABLE I
EXPERIMENTAL PARAMETERS

Parameters	Specific values	Parameters	Specific values
R_c	115.625μm	d_{inj}	20.628μm
R_{zp}	83.597μm	θ_{inj}	25.238°

D. Micropipette Approaching the Optimal Spindle Removal Position Process

The process of approaching the optimal spindle removal position with a micropipette is illustrated in Fig. 9. Initially, oocyte fixation and micropipette preparation are conducted during the setup phase of the experiment. Once the experiment began, the micropipette applied vertical pressure to the oocyte from the 3 o'clock direction, while simultaneously recording the force-displacement curve. Following this, initial values for variables in the NMSD system are set based on the acquired experimental force-displacement data. In the simulation phase, with consistent insertion speed and micropipette displacement conditions, forces on springs and dampers across the NMSD system's edges are calculated. The NMSD model parameters are then adjusted to match the force-displacement curve obtained from experiments. Calibration concluded when the similarity between experimental and simulated force-displacement curves exceeds 0.999 at each data point.

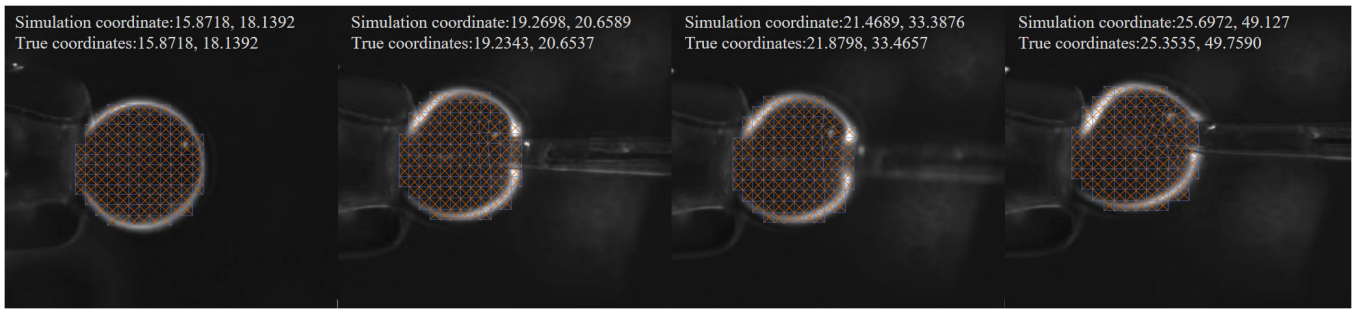

Fig. 8. Simulation process of the micropipette approaching the predicted position of the spindle.

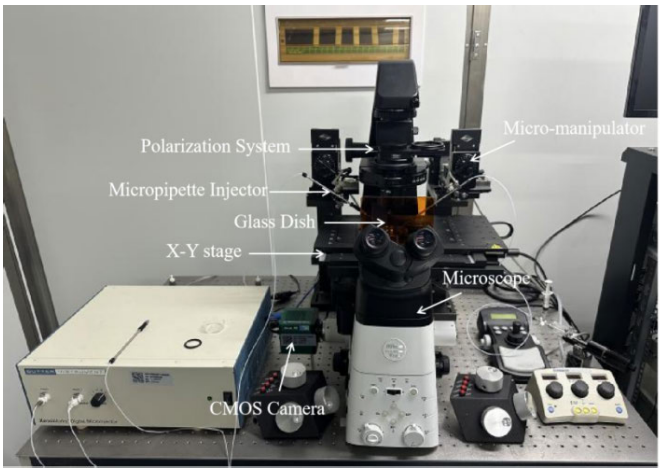

Fig. 9. Micro-manipulation system.

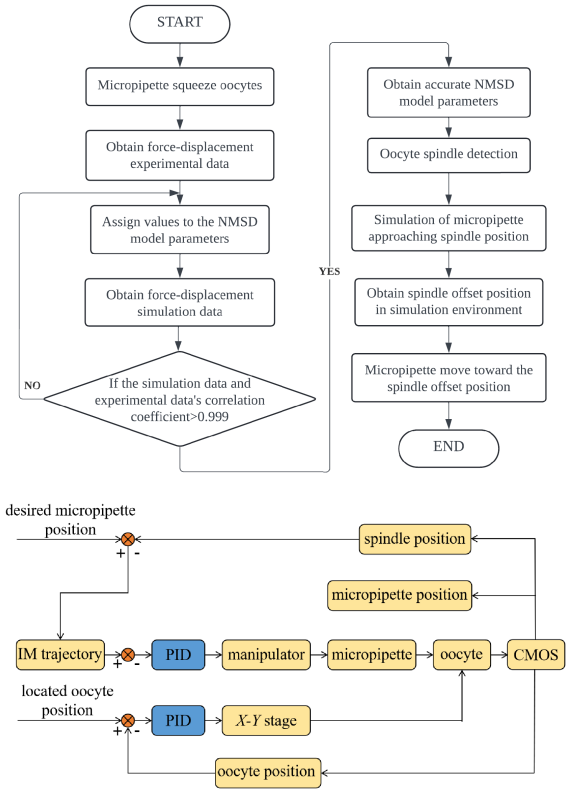

Fig. 10. Flowchart of micropipette approaching predicted spindle position and block diagram of micropipette control method.

Post-calibration, the micropipette is maneuvered within the NMSD model to determine the spindle position after displacement. Subsequently, the experiment guided the micropipette towards these displaced spindle coordinates, thereby completing the approach to the optimal spindle removal position.

The position of the micropipette relative to the oocyte spindle is adjusted based on spindle position feedback, with control adjustments made relative to the control amount of the previous moment. The position tracking error e is defined as:

$$e = x_d - x \tag{9}$$

where x_d is the desired micropipette movement trajectory (the line connecting the micropipette mouth and the optimal spindle removal point), and x is the actual position of the micropipette. The PID control is expressed as follows:

$$\begin{aligned} u(t) = u(t-T) + K_p[e(t) - e(t-T)] + K_i e(t) \\ + K_d[e(t) - 2e(t-T) + e(t-2T)] \end{aligned} \tag{10}$$

where T is the sampling time interval, and $u_{(t-T)}$ denotes the control variable in the previous time step. K_p, K_i, and K_d are the positive gains to be designed.

III. Experiment Results

A. System Setup

The proposed micro-manipulation system is integrated based on a motorized inverted microscope (TiE, Nikon) with a 20× objective lens for micro-manipulation. A polarization system (MEY10031 TI2-C-SO, Nikon) is placed for oocyte spindle imaging. A motorized X-Y-Z micromanipulator (MP285, Sutter) with a motion range of 25 mm and a positioning resolution of 0.04 μm, connects with the micropipette holder and drives the micropipette to move. A motorized X-Y stage (ProScan III, Prior) with a motion range of 120 mm ×80 mm and a positioning resolution of 0.05 μm, carries the glass dish (LQ-1177-60) with the porcine oocytes and moves the oocytes into the field of view (FOV) of the microscope in the experiment. The controllers of the motorized micromanipulator and motorized stage are connected to the computer via a serial interface. The software of the proposed micro-manipulation system calls the functions in the software development toolkit to control the motorized devices. An micropipette is attached to a digital microinjector

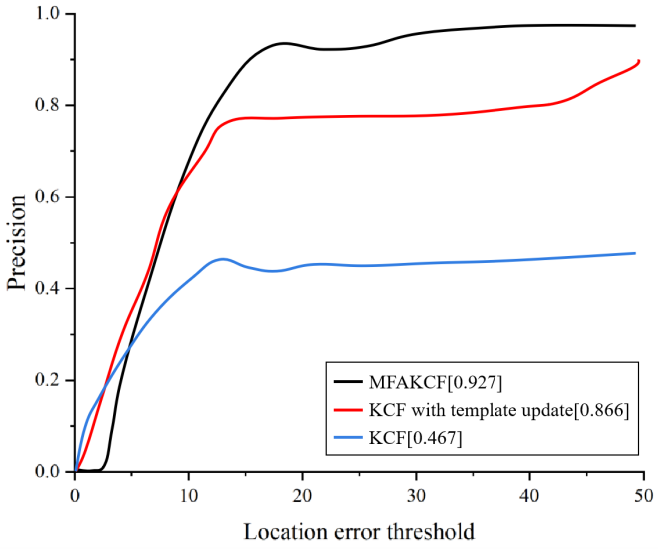

Fig. 11. Spindle tracking algorithm precision-threshold curve.

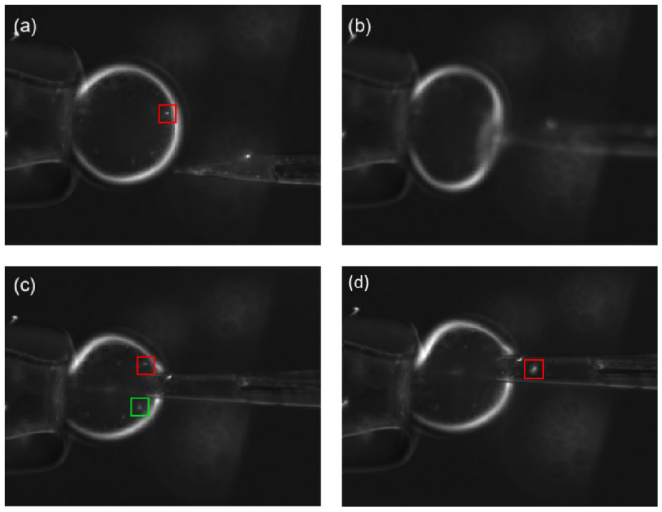

Fig. 12. The qualitative tracking results. (a) Initial position of the spindle. (b) Spindle displacement due to local transparency changes in the oocyte during the insertion of the injection micropipette, leading to loss of spindle position. (c) Spindle reappearance (red box) after the oocyte is punctured, with accompanying fat vesicles (green box) causing interference and affecting tracking accuracy. (d) Successful spindle identification and tracking until its removal from the oocyte.

(XenoWorks BRE, Sutter). A CMOS camera (Iris-9, Teledyne Photometrics) is mounted on the microscope for visual feedback. Fig. 9. shows the prototype of the micro-manipulation system.

The holding micropipette(HM) was made from a borosilicate glass tube with an outer diameter of 1 mm and inner diameter of 0.6 mm. The glass tube was drawn by a micropipette puller (P-97, Sutter Instrument) and was then forged into a microtube with a diameter of 50-80 μm by a forging needle instrument (MF-900, Narishige). Finally, the opening was melted by a professional with an alcohol lamp to make the needle smooth. The micropipette was purchased from CooperSurgical (TPC, LBC-OD20BA90, Australia). The tip had an outer diameter of 20 μm and tip angle of 45°.

B. Spindle Recognition and Tracking Results

In our recognition and tracking experiment, we employed the MFAKCF algorithm to achieve real-time detection and monitoring of spindle movement. The tracking process involved using a micropipette to puncture oocytes and maneuver them towards the spindle's position, resulting in an average displacement of 35 μm. Key evaluation metrics for algorithm performance included accuracy and success rate. We computed the percentage of frames where the pixel distance between estimated and ground truth object positions was below a predefined threshold, generating precision values corresponding to different thresholds and plotting precision-recall curves.

A comparative analysis of the proposed tracking algorithm, represented by the black line in Fig. 11, shows significant improvements over our previous tracking algorithm, depicted as the blue line. The integration of multiple features has notably enhanced the robustness of the algorithm, especially in the presence of interference, as illustrated by the red line in Fig. 11. The adaptive template updating function further proves effective under challenging conditions, such as fluctuating microscope light intensity, changing shapes of genetic material, and interference from lipid vesicles.

The experimental results highlight that the MFAKCF algorithm demonstrated superior tracking performance when assessed using the precision-threshold curve at various threshold settings. Specifically, the algorithm achieved an average tracking accuracy of 92.84% and a 100% success rate, marking improvements of 45.63% and 49.89% over the original KCF algorithm, respectively, as shown in Fig. 11. These advancements are primarily attributed to the incorporation of two key modules: the adaptive fusion module and the adaptive update module. The adaptive fusion module enables dynamic adjustment to scene-specific features, effectively leveraging multi-feature information. Meanwhile, the adaptive update module enhances the model's ability to learn and adapt over time, reducing the risk of model drift and further improving overall tracking performance. Qualitative tracking results are presented in Fig. 12.

C. Experimental Results of Predict Optimal Removal Spindle Position

This section focuses on the experiment to predict the optimal spindle removal point and the accuracy of the prediction. We predict the optimal removal positions for spindle bodies in 20 sets of oocytes. The prediction process is illustrated in Fig. 13. Initially, oocytes are fixed and micropipette prepared before the experiment commences. During the experiment, micropipette exert vertical pressure on the oocytes, concurrently recording force-displacement experimental data $[f_{e1}, f_{e2}, f_{e3}, \ldots f_{en}]$, as shown in Table II. Subsequently, initial values are assigned to variables in the NMSD system based on the force-displacement data obtained. Following this, using the same micropipette speed(30μm/s) and displacement (65μm) conditions in a simulated environment, the resultant forces on each spring and damper in the NMSD system are computed. Thereafter, adjusting the parameters of the NMSD

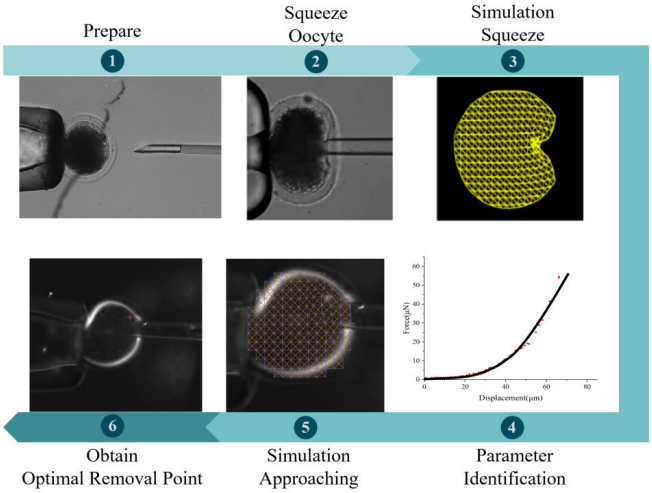

Fig. 13. Experimental process of micropipette approaching the optimal spindle removal position.

TABLE II
THE FORCE-DISPLACEMENT DATA OBTAINED FROM THE EXPERIMENT AND SIMULATION

Displacement μm	Force(expriment) μN	Force(simulation) μN
0	0	0
3.5	0.00028	0.00009
6.25	0.00252	0.00019
12.5	0.08468	0.08254
14.375	0.06413	0.067154
16.25	0.63407	0.62957
19.375	1.02889	1.02158
23.75	2.22705	2.24646
28.125	3.45531	3.46787
33.125	5.92187	5.86723
41.25	10.44089	10.75634
53.25	13.48404	13.38373
57.75	28.38455	30.27377
62.375	55.32843	55.38837

model based on the force-displacement curves obtained from the simulation $[f_{x1}, f_{x2}, f_{x3}, \ldots f_{xn}]$, simulating data alongside experimental results, and refining model parameters, where$d_0 = 20.182Ns/m$, $d_1 = 10000Nm/s^2$, $k_1 = 2.5N$, $k_2 = 95.9738N$. Once calibration of the model parameters is complete, experiments in the simulated environment proceed to simulate the micropipette approaching the spindle bodies, capturing the coordinates of spindle force deviation within the oocytes, representing the optimal spindle removal point.

D. Experimental Results of Micropipette Approaching the Optimal Removal Spindle Position

To validate the effectiveness of our proposed method for optimal spindle removal using micropipette manipulation, this section compares it with invisible aspiration and a previously developed method [8], focusing on the distance between the micropipette tip and the spindle position. We also examine the success rate of genetic material removal and the volume of cytoplasm removed by reducing the internal pressure of the micropipette.

Firstly, oocytes were randomly divided into three groups, 20 in each group. They underwent procedures using our proposed predictive positioning method for optimal spindle approach (see Fig. 13), a previous automated invisible aspiration method for approaching the nucleus [8], and a traditional invisible aspiration method. First, the polarizer was rotated to make the spindle in the oocyte visible, and the spindle of the oocyte was rotated to the 2 o'clock position in the focal plane. Subsequently, the micropipette was guided along the X-axis from the 3 o'clock direction to compress and penetrate the oocyte. During this process, variations in local transparency of the oocyte may cause interference from lipid droplets, which were further identified using the MFAKCF algorithm to accurately track the spindle. After determining the actual spindle position, the NMSD model predicted the optimal spindle removal position. Finally, the micropipette was controlled to move towards the predicted optimal spindle removal position. In the case of the other two methods, the spindle of the oocyte was rotated to the 2 o'clock position, and an experienced operator guided the micropipette along a trajectory to approach the nucleus. The final experimental results show that the average accuracy of the offset coordinates predicted by the NMSD model in this paper and the coordinates obtained by using a micropipette to precisely approach the spindle reached 97.26%, with an average error of only 0.4μm.

These three methods aim to minimize the distance between the micropipette tip and the genetic material (spindle or nucleus) while ensuring complete removal of the genetic material and minimizing cytoplasmic loss. To evaluate the superiority of our proposed method, we performed statistical analysis on the average distance between the micropipette tip and the spindle after applying each method. The results demonstrate that our approach, by optimizing oocyte orientation and designing ideal removal points, reduced the average distance between the micropipette tip and the spindle by 68%. Furthermore, to assess the effectiveness of our method in reducing unnecessary cytoplasmic loss, we used cytoplasmic loss as a metric, defined as the ratio of the volume of removed spindle and surrounding cytoplasm to the total cytoplasmic volume. The total cytoplasmic volume was approximated by treating the oocyte (excluding the zona pellucida) as a sphere, while the removed cytoplasmic volume was approximated as a cylinder with a diameter equal to the inner diameter of the micropipette (20 μm). Using previous methods, the removed cytoplasmic volume (shown in the green box in Fig. 14(a)) was 6.9% of the total oocyte volume by reducing the internal pressure of the micropipette. In contrast, our proposed method, illustrated in the red box in Fig. 14(b), reduced the cytoplasmic removal to 4.5%, a 34.78% decrease from the previous method and significantly lower than the 30% achieved with invisible aspiration. The comparative results of the three methods are shown in Fig. 14(c), indicating that our method achieves the smallest average cytoplasmic removal. Lastly, as depicted in Fig. 14(d), our method enabled the visualization of spindle with a 100% success rate in spindle removal, surpassing the previous success rate of 92.3% and the traditional invisible aspiration success rate of 77.1%.

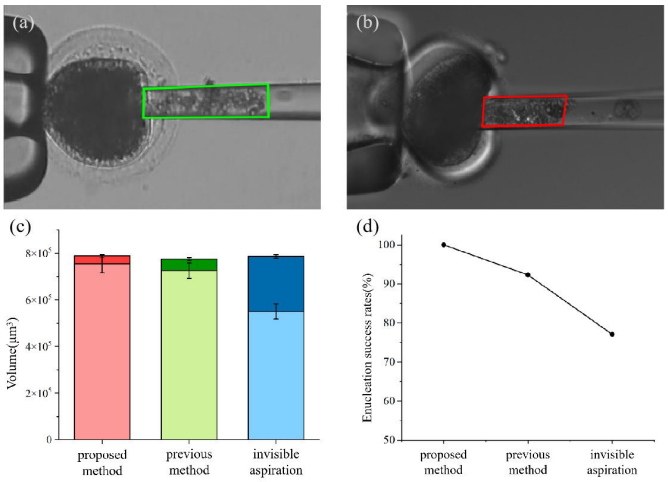

Fig. 14. Experimental Results. (a). The volume of cytoplasm removed by previous methods. (b). The volume of cytoplasm removed by proposed method. (c). Comparison of average removal volumes of the proposed method, previous methods and invisible aspiration. (d). The obtained enucleation success rate for proposed method, previous method and bind aspiration.

IV. Discussion

This study proposes a novel method involving predictive positioning to determine the optimal spindle removal location for robotic SCNT applications. The method addresses the inherent challenges of visualizing genetic material encountered in traditional invisible aspiration techniques. By integrating a polarization imaging module, our study successfully enhanced the visibility of spindles in oocytes. However, the current polarization imaging system is limited to observing meiotic spindles and cannot visualize differentiated nuclei or polar bodies. Therefore, culturing reconstructed embryos and calculating the blastocyst rate are essential steps for evaluating the feasibility of reconstructed embryos using the spindle removal technique described in this study, thereby confirming its applicability for robotic nuclear transfer applications.

From the perspective of time efficiency, the proposed method demonstrated a significant reduction in spindle visualization time. For structurally intact in vitro-matured oocytes cultured for 36 hours, the spindle visualization process averaged 20±5 seconds, compared to the over 30 minutes typically required for staining and imaging preparation in traditional fluorescence-based methods. This substantial reduction in time, coupled with the elimination of potential phototoxicity, highlights the efficiency and practicality of the proposed system, particularly for live-cell applications requiring rapid and non-invasive spindle visualization.

In this study, the Nonlinear Mass-Spring-Damper (NMSD) model integrates nonlinear springs and direct velocity dampers, enhancing its accuracy in simulating the mechanical properties of oocytes compared to finite element models. The adjustable parameters of the NMSD model facilitate calibration, making it highly suitable for real-time biological experiments. The accurate prediction of spindle displacement enables reliable estimation of spindle offset and confirms the effectiveness of the proposed NMSD-based micromanipulator approach for approaching spindles in oocytes. This method demonstrates improved nuclear removal success rates and reduced cytoplasmic volume loss, validating its efficacy for precise spindle manipulation.

Although this study focuses primarily on porcine oocytes, the proposed method exhibits potential for broader applicability to other cell types. The mechanical parameters of the NMSD model, including spring constants and damping coefficients, can be recalibrated for other cell types, such as murine or bovine oocytes, by performing fixed-cell puncture experiments to derive force-displacement curves. Future work will aim to extend the method to additional cell types, further validating its generalizability and addressing challenges such as differences in spindle morphology, cell size, and mechanical stiffness.

V. Conclusion

In the context of SCNT, precise removal of the cell nucleus presents a critical technological challenge. This study successfully achieved precise tracking of the oocyte genetic material (spindle) using a polarized light imaging system and a MFAKCF visual tracking algorithm, achieving a tracking success rate of 100%. Additionally, an improved NMSD model effectively simulated the mechanical properties of live cells and predicted spindle position shifts under various experimental conditions through simulation. Ultimately, this research proposes an optimal approach for approaching the nucleus with a micromanipulator based on predictive positioning. Experimental validation demonstrated a prediction accuracy of 97.26% and an average positional error of only 0.4 μm. Using this approach, cytoplasm loss can be reduced to 4.5% and achieve a 100% enucleation success rate. This method provides reliable technical support for reducing cytoplasmic loss and optimizing SCNT procedures.

References

[1] S. Ijaz and I. Hyun, "Somatic cell nuclear transfer: The promise and the perils," *Current Stem Cell Rep.*, vol. 1, no. 4, pp. 215–218, Dec. 2015.

[2] Y. Zhang et al., "Automated dissection of intact single cell from tissue using robotic micromanipulation system," *IEEE Robot. Autom. Lett.*, vol. 8, no. 8, pp. 4705–4712, Aug. 2023.

[3] M.-Z. Sun et al., "Intracellular strain evaluation-based oocyte enucleation and its application in robotic cloning," *Engineering*, vol. 24, pp. 73–83, May 2023.

[4] A. D. Alegria et al., "High-throughput genetic manipulation of multicellular organisms using a machine-vision guided embryonic microinjection robot," *Genetics*, vol. 226, no. 4, Apr. 2024, Art. no. iyae025.

[5] C. K. Schmidt, M. Medina-Sánchez, R. J. Edmondson, and O. G. Schmidt, "Engineering microrobots for targeted cancer therapies from a medical perspective," *Nature Commun.*, vol. 11, no. 1, pp. 5618–5636, Nov. 2020.

[6] F. Pan, Y. Jiao, S. Chen, L. Xing, and D. Sun, "Deep learning-enhanced dual-module large-throughput microinjection system for adherent cells," *IEEE Trans. Autom. Sci. Eng.*, vol. 20, no. 4, pp. 2409–2422, Apr. 2023.

[7] S. Hua et al., "Effects of the removal of cytoplasm on the development of early cloned bovine embryos," *Animal Reproduction Sci.*, vol. 126, nos. 1–2, pp. 37–44, Jun. 2011.

[8] Q. Zhao et al., "Robotic label-free precise oocyte enucleation for improving developmental competence of cloned embryos," *IEEE Trans. Biomed. Eng.*, vol. 68, no. 8, pp. 2348–2359, Aug. 2021.

[9] C. P. Silva, K. Kommineni, R. Oldenbourg, and D. L. Keefe, "The first polar body does not predict accurately the location of the metaphase II meiotic spindle in mammalian oocytes," *Fertility Sterility*, vol. 71, no. 4, pp. 719–721, Apr. 1999.

[10] D. Keefe, L. Liu, W. Wang, and C. Silva, "Imaging meiotic spindles by polarization light microscopy: Principles and applications to IVF," *Reproductive Biomed. Online*, vol. 7, no. 1, pp. 24–29, Jan. 2003.

[11] J. N. Caamaño et al., "Use of polarized light microscopy in porcine reproductive technologies," *Theriogenology*, vol. 76, no. 4, pp. 669–677, Sep. 2011.

[12] S. Schuck and K. Simons, "Polarized sorting in epithelial cells: Raft clustering and the biogenesis of the apical membrane," *J. Cell Sci.*, vol. 117, no. 25, pp. 5955–5964, Dec. 2004.

[13] E. Asa, R. Tabatabaee, A. Farrokhi, and R. Nejatbakhsh, "Relationship between meiotic spindles visualization and intracytoplasmic sperm injection outcomes in human oocytes," *Anatomy Cell Biol.*, vol. 50, no. 1, pp. 26–32, 2017.

[14] Z. Liu et al., "Cloning of macaque monkeys by somatic cell nuclear transfer," *Cell*, vol. 174, no. 4, pp. 881–887, Jun. 2018.

[15] X.-F. Sun, W.-H. Zhang, X.-J. Chen, G.-H. Xiao, W.-Y. Mai, and W.-H. Wang, "Spindle dynamics in living mouse oocytes during meiotic maturation, ageing, cooling and overheating: A study by polarized light microscopy," *Zygote*, vol. 12, no. 3, pp. 241–249, Aug. 2004.

[16] Z. Li, Y. Jian, J. Hu, C. Zhang, X. Meng, and J. Liu, "SpindlesTracker: An automatic and low-cost labeled workflow for spindle analysis," *IEEE J. Biomed. Health Informat.*, vol. 27, no. 8, pp. 4098–4109, Aug. 2023.

[17] T. Xu, Y. Guan, J. Liu, and X. Wu, "Image-based visual servoing of helical microswimmers for planar path following," *IEEE Trans. Autom. Sci. Eng.*, vol. 17, no. 1, pp. 325–333, Jan. 2020.

[18] K. Miyoshi, S. J. Rzucidlo, J. R. Gibbons, S. Arat, and S. L. Stice, "Development of porcine embryos reconstituted with somatic cells and enucleated metaphase I and II oocytes matured in a protein-free medium," *BMC Develop. Biol.*, vol. 1, no. 1, p. 12, Jul. 2001.

[19] J. Wang, X. Li, J. Zheng, and D. Sun, "Dynamic path planning for inserting a steerable needle into a soft tissue," *IEEE/ASME Trans. Mechatronics*, vol. 19, no. 2, pp. 549–558, Apr. 2014.

[20] L. Wijayarathne, Z. Zhou, Y. Zhao, and F. L. Hammond, "Real-time deformable-contact-aware model predictive control for force-modulated manipulation," *IEEE Trans. Robot.*, vol. 39, no. 5, pp. 3549–3566, 2023.

[21] G. Flé, E. Van Houten, G. Rémillard-Labrosse, G. FitzHarris, and G. Cloutier, "Imaging the subcellular viscoelastic properties of mouse oocytes," *Proc. Nat. Acad. Sci. USA*, vol. 120, no. 21, May 2023, Art. no. e2213836120.

[22] B. Ambruosi et al., "Cytoplasmic lipid droplets and mitochondrial distribution in equine oocytes: Implications on oocyte maturation, fertilization and developmental competence after ICSI," *Theriogenology*, vol. 71, no. 7, pp. 1093–1104, Apr. 2009.

[23] Z. Wang, X. Zhao, X. Zhao, and Y. Liu, "Detection of oocyte nucleus motion based on mean drift algorithm," in *Proc. Mach. Learn., Multi Agent Cyber Phys. Syst.*, Tianjin, China, Jan. 2023, pp. 348–355.

[24] B. González-Bermúdez, G. V. Guinea, and G. R. Plaza, "Advances in micropipette aspiration: Applications in cell biomechanics, models, and extended studies," *Biophysical J.*, vol. 116, no. 4, pp. 587–594, Feb. 2019.

[25] J. F. Henriques, R. Caseiro, P. Martins, and J. Batista, "High-speed tracking with kernelized correlation filters," *IEEE Trans. Pattern Anal. Mach. Intell.*, vol. 37, no. 3, pp. 583–596, Mar. 2015.

[26] T. L. Nguyen, E. R. Polanco, A. N. Patananan, T. A. Zangle, and M. A. Teitell, "Cell viscoelasticity is linked to fluctuations in cell biomass distributions," *Sci. Rep.*, vol. 10, no. 1, p. 7403, May 2020.

[27] E. Keeve, S. Girod, P. Pfeifle, and B. Girod, "Anatomy-based facial tissue modeling using the finite element method," in *Proc. 7th Annu. IEEE Visualizat.*, San Francisco, CA, USA, Oct. 1996, pp. 21–28.

[28] S. S. Tabatabaei, M. R. Dehghan, and H. A. Talebi, "Real-time prediction of soft tissue deformation; a non-integer order modeling scheme and a practical verification for the theoretical concept," *Chaos, Solitons Fractals*, vol. 155, Feb. 2022, Art. no. 111633.

[29] G. R. Joldes, A. Wittek, and K. Miller, "Suite of finite element algorithms for accurate computation of soft tissue deformation for surgical simulation," *Med. Image Anal.*, vol. 13, no. 6, pp. 912–919, Dec. 2009.

[30] R. Lewandowski and B. Chorążyczewski, "Identification of the parameters of the Kelvin–Voigt and the Maxwell fractional models, used to modeling of viscoelastic dampers," *Comput. Struct.*, vol. 88, nos. 1–2, pp. 1–17, Jan. 2010.

[31] Y. Zhang et al., "Mechanical force estimation based on visual cell deformation and improved point-load model," *IEEE Trans. Instrum. Meas.*, vol. 72, pp. 1–9, 2023.

[32] M. Ammi, H. Ladjal, and A. Ferreira, "Evaluation of 3D pseudo-haptic rendering using vision for cell micromanipulation," in *Proc. IEEE/RSJ Int. Conf. Intell. Robots Syst.*, Beijing, China, Oct. 2006, pp. 2115–2120.

[33] E. Basafa and F. Farahmand, "Real-time simulation of the nonlinear visco-elastic deformations of soft tissues," *Int. J. Comput. Assist. Radiol. Surg.*, vol. 6, no. 3, pp. 297–307, May 2011.

[34] J.-M. Schwartz, M. Denninger, D. Rancourt, C. Moisan, and D. Laurendeau, "Modelling liver tissue properties using a non-linear visco-elastic model for surgery simulation," *Med. Image Anal.*, vol. 9, no. 2, pp. 103–112, Apr. 2005.

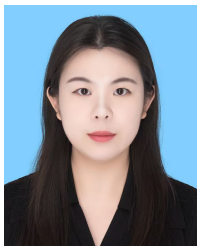

Zuqi Wang was born in 1998. She received the bachelor's degree in automation from Huazhong Agricultural University, Hubei, China, in 2020, and the master's degree in artificial intelligence from Nankai University, Tianjin, China, in 2024. Her graduate studies were mostly focused on robotic micro-manipulation and computer vision.

Yujie Zhang was born in 1998. He received the bachelor's degree in intelligent science and technology from Nankai University, Tianjin, China, in 2020, where he is currently pursuing the Ph.D. degree in control science and engineering. His research interests include micromanipulation and control theory.

Yidi Zhang was born in 1997. She received the bachelor's degree in automation from Hebei University of Technology, Tianjin, China, in 2019. She is currently pursuing the Ph.D. degree with the School of Artificial Intelligence, Nankai University, Tianjin. Her current research interests include micromanipulation and micro- and nanorobotics.

Detian Zhang received the bachelor's degree in automation from Harbin Institute of Technology in 2022. He is currently pursuing the master's degree with the College of Artificial Intelligence, Nankai University, Tianjin, China. His research interests include robotic automated enucleation, simulation analysis, and microsystems.

Zhaotong Chu received the bachelor's degree in electrical engineering and automation from the University of Jinan, Jinan, China, in 2022. He is currently pursuing the Ph.D. degree with the College of Artificial Intelligence, Nankai University, Tianjin, China. His current research interests include micromanipulators and microsystems.

Qili Zhao (Member, IEEE) received the Ph.D. degree in control theory and control engineering from Nankai University, Tianjin, China, in 2014. He finished his first Post-Doctoral Research with the Robotics and Mechatronics Research Laboratory, Department of Mechanical and Aerospace Engineering, Monash University, Melbourne, VIC, Australia, from 2014 to 2015. He was a Post-Doctoral Fellow with the Advanced Micro and Nanosystems Laboratory, Department of Mechanical and Industrial Engineering, Toronto University, Toronto, ON, Canada, from 2015 to 2018. He is currently an Associate Professor with the College of Artificial Intelligence, Nankai University. His research interests include robotic patch clamp, robotic cell manipulation, and robotic cell measurement.

Mingzhu Sun (Member, IEEE) received the B.S. degree in computer science and technology, the M.S. degree in computer application, and the Ph.D. degree in control theory and control engineering from Nankai University, Tianjin, China, in 2003, 2006, and 2009, respectively. She joined as a Faculty Member with Nankai University, in 2009. She is currently a Professor and the Deputy Director of the Institute of Robotics and Automatic Information System. Her research interests include micromanipulator, image processing, and computer vision.

Maosheng Cui received the B.A. degree from the Department of Animal Science, Anhui Technological College, Hefei, China, in 2003, the M.A. degree from the Animal Science College, Yunnan Agricultural University, Kunming, Yunnan, China, in 2006, and the Ph.D. degree from the Animal Science College, Chinese Agricultural University, Beijing, China, in 2009. He was a Post-Doctoral Researcher with Chinese Academy of Agricultural Sciences from 2011 to 2013. He is with Tianjin Animal Sciences Institute, Tianjin, China, as an Associate Investigator in the study and application of reproduction biotechnology in domestic animals.

Xin Zhao (Member, IEEE) received the B.S. degree in control theory and control engineering from Nankai University, Tianjin, China, in 1991, the M.S. degree in control theory and control engineering from Shenyang Institute of Automation, CAS, Shenyang, China, in 1994, and the Ph.D. degree in control theory and control engineering from Nankai University in 1997. He joined as a Faculty Member with Nankai University in 1997, where he is currently a Professor and the Dean of the College of Artificial Intelligence. His research interests include micromanipulators, microsystems, and mathematical biology.

Yaowei Liu (Member, IEEE) received the B.Eng. degree in automation and the Ph.D. degree in control theory and control engineering from Nankai University, Tianjin, China, in 2013 and 2019, respectively. He was a Post-Doctoral Researcher with the College of Artificial Intelligence, Nankai University, in 2023, where he is currently an Assistant Professor. His research interests include robotic cell micromanipulation and robotic cell measurement.